metals

Article

Effect of Friction Surfacing on the Microstructure and Corrosion Behavior of CoCrFeMnNi High-Entropy Alloy

Weiwei Chang [1,2,†], Feng Yuan [1,2,†], Jingtao Ren [1,2], Zhongyu Wu [1,2], Min Zhou [3,4], Hongchang Qian [1,2,*], Hao Zhang [1,2], Dawei Guo [3,4], Tong Sun [2,5,*], Chi Tat Kwok [4], Lap Mou Tam [3,4] and Dawei Zhang [1,2,5]

1 National Materials Corrosion and Protection Data Center, Institute for Advanced Materials and Technology, University of Science and Technology Beijing, Beijing 100083, China; cww1995210xy@sina.com (W.C.)
2 BRI Southeast Asia Network for Corrosion and Protection (MOE), Shunde Innovation School of University of Science and Technology Beijing, Foshan 528399, China
3 IDQ Science and Technology Development (Hengqin, Guangdong) Co., Ltd., Zhuhai 519031, China
4 Department of Electromechanical Engineering, University of Macau, Macau 999078, China
5 School of Advanced Materials Innovation, University of Science and Technology Beijing, Beijing 100083, China
* Correspondence: qianhc@ustb.edu.cn (H.Q.); tongsun@ustb.edu.cn (T.S.)
† These authors contributed equally to this work.

Abstract

In recent years, CoCrFeMnNi high-entropy alloy (HEA) has attracted considerable attention owing to its exceptional mechanical properties, thermal stability and corrosion resistance. Friction surfacing (FS), as a solid-state additive manufacturing technology that can avoid point defects such as pores, has great application potential in the fabrication of HEA coatings. However, relevant research has been extremely limited so far. In this article, a CoCrFeMnNi HEA coating was successfully fabricated on 304 stainless steel substrates via FS. The microstructure and corrosion behavior of as-cast HEA, solution-treated HEA and HEA coating prepared by FS were systematically analyzed. The results showed that the as-cast alloy exhibited severe dendritic segregation of Mn and Ni elements, with large-sized $MnCr_2O_4$-MnS composite inclusions widely distributed. Solution treatment could alleviate this segregation and partially suppress the corrosion rate. In contrast, the thermo-mechanical coupling imposed by FS eliminated the dendritic segregation and promoted compositional homogeneity. Moreover, FS effectively fragments the inclusions in the HEA, leaving only small-sized $MnCr_2O_4$ observable. These effects substantially reduced the defect density in the passive film on the FSed-coating surface, leading to a marked enhancement in corrosion resistance. The corrosion current density (i_{corr}) of the coating decreased from 0.55 μA/cm^2 in the as-cast state to 0.11 μA/cm^2, and the pitting potential increased from −120.3 mV to 125.7 mV.

Keywords: friction surfacing; high entropy alloy; corrosion resistance; microstructural evolution; CoCrFeMnNi

Check for updates

Academic Editor: Dariusz Rozumek

Received: 19 August 2026
Revised: 28 September 2026
Accepted: 1 October 2026
Published: 6 October 2026

Copyright: © 2026 by the authors. Licensee MDPI, Basel, Switzerland. This article is an open access article distributed under the terms and conditions of the Creative Commons Attribution (CC BY) license.

1. Introduction

High concentrations of chloride ions will readily induce rapid failure of engineering materials during service, ultimately leading to safety incidents [1,2]. Therefore, corrosion protection in marine environments represents an urgent and critical engineering challenge [3,4]. To prolong the service life of materials under such conditions, researchers have proposed and implemented various novel strategies for developing corrosion-resistant materials. In recent years, high entropy alloys (HEAs) have emerged as a new alloy design

paradigm, attracting considerable attention owing to their exceptional mechanical properties, thermal stability and corrosion resistance [5–9]. Unlike conventional alloys, which are based on only one principal element, HEAs consist of multiple principal elements in near-equimolar proportions [10]. The resulting high configurational entropy tends to suppress the formation of intermetallic compounds, favoring the formation of one or two simple solid-solution phases instead. Among these, equiatomic CoCrFeMnNi HEA with a single-phase face-centered cubic (FCC) structure has been extensively researched [11,12]. It was reported that CoCrFeMnNi HEA possessed an excellent combination of fracture toughness and strength at cryogenic temperatures, as well as superior resistance to hydrogen embrittlement [13–15]. In terms of corrosion resistance, the high Mn content in CoCrFeMnNi HEA tends to cause elemental segregation during the melting process, resulting in a weaker spontaneous passivation capability [16]. Additionally, the high cost of bulk HEAs restricts their widespread application. Consequently, fabricating high-quality CoCrFeMnNi HEA coatings on conventional substrates became an economically viable strategy.

Additive manufacturing is an effective approach for depositing alloy coatings, including HEA coatings, with key advantages of high design flexibility and strong metallurgical bonding. At present, numerous previous studies have reported the mechanical properties of CoCrFeMnNi HEA fabricated by various additive manufacturing methods [17–19]. Research on the influence of additive manufacturing on the microstructural evolution and the correlation between the microstructure and corrosion performance remains limited. Ye et al. fabricated a CoCrFeMnNi HEA coating via laser cladding and found that its corrosion resistance in 3.5 wt.% NaCl solution was inferior to that of 304 stainless steel [20]. This degradation was attributed to the existence of (Mn, Ni)-rich dendritic regions, where the spontaneously formed passive film underwent preferential breakdown, thereby initiating localized corrosion. Xu et al. compared the corrosion resistance of CoCrFeMnNi HEA fabricated by selective laser melting (SLMed HEA) with that of the as-cast counterpart [21]. The SLMed HEA exhibited a more uniform elemental distribution and finer grains, which promoted the formation of a more stable and protective passive film. Nevertheless, its polarization curve in 3.5 wt.% NaCl solution displayed no distinct pitting potential, indicating that the presence of (Mn, Ni)-rich regions continued to severely compromise the pitting resistance. These findings suggested that suppressing the segregation of Mn and Ni elements in CoCrFeMnNi HEA was essential for further enhancing the corrosion performance [22].

Friction surfacing (FS), as one type of solid-state additive manufacturing technology derived from friction stir welding (FSW), has been applied to the coating fabrication of various materials, including magnesium alloys, aluminum alloys and stainless steels [23–26]. FS involves the high-speed rotation of a consumable rod, which generates frictional heat at the rod tip and induces severe plastic deformation (SPD). The subsequent traverse movement deposits the softened material onto the substrate. As the processing temperature only reaches approximately 80% of the melting point, FS can avoid the defects typically caused by fusion-based processing, including pores and cracks, thus yielding a dense and defect-free metal layer [27–29]. In our previous study, we demonstrated that FS could effectively fragment the NbS inclusions in 17-4PH stainless steel through SPD, which enhanced the integrity of the passive film and significantly improved the pitting resistance [26]. Additionally, high processing temperature promoted the solid-solution of nano-scale Cu-rich precipitates, further increasing the homogeneity of composition for the passive film. These results showed that FS held considerable potential to serve as a viable method for fabricating high-performance HEA coatings. Nartu et al. investigated the microstructural evolution and the hardness change of $Al_{10}Cr_{12}Fe_{35}Mn_{23}Ni_{20}$ HEA after FS [30]. They revealed

that SPD imposed during FS processing caused the fragmentation of body-centered cubic (BCC) dendrites into smaller fragments. A substantial improvement in hardness from 177 HV to 283 HV, driven by Hall-Petch strengthening, was observed, attributed to the resulting microstructural refinement through FS. Nevertheless, studies on the FS of HEAs and its influence on the corrosion resistance of HEAs remain extremely limited to date.

Herein, we successfully fabricated CoCrFeMnNi HEA coatings on the 304 stainless steel substrates through FS, and the effect of FS on the microstructure and corrosion resistance of the HEA coatings was elaborated. The microstructure of each specimen was characterized using X-ray diffraction (XRD) and scanning electron microscopy (SEM) coupled with an energy-dispersive X-ray spectrometry (EDS) detector and an electron backscatter diffraction (EBSD) detector. Linear polarization resistance (LPR) testing, electrochemical impedance spectroscopy (EIS) and potentiodynamic polarization (PDP) were employed to investigate the corrosion behavior of various HEA samples in 3.5 wt.% NaCl solution. The semiconductor characteristics and compositions of the passive film formed on each sample were analyzed by the Mott-Schottky test and X-ray photoelectron spectroscopy (XPS), respectively. The corroded surface morphology was also observed using SEM to identify the pitting initiation sites.

2. Experimental Methods

2.1. Materials

As-cast CoCrFeMnNi cylindrical ingot (Φ80 mm × 240 mm) was obtained by arc melting using high-purity Co, Cr, Fe, Mn and Ni elemental materials (>99.9%) in a pure argon atmosphere. The ingots underwent 8 remelting cycles at a current of 480 A to ensure uniform composition. Table 1 presents the chemical composition (wt.%) of the ingot. Figure 1 shows the schematic diagram of HEA fabrication, solution treatment and FS. For solid-solution specimens, the as-cast ingot was wire-cut into samples with dimensions of 10 mm × 10 mm × 3 mm. They were then solution-treated at 1100 °C for 1 h in a vacuum tube furnace (OTF-1200X, HF-Kejing, Hefei, China), followed by rapid water quenching to room temperature. For FS coatings, the ingot was wire-cut into consumable rods with a diameter of 15 mm and a length of 75 mm. FS processing was conducted using a commercial FSW machine (FSW-TS-M16, China FSW Center, Beijing, China) with a spindle speed (n) of 1000 rpm, a processing speed (v) of 40 mm/min and a constant feeding rate (v_z) of 20 mm/min. Two argon gas distributors were positioned on both sides of the processing area to achieve rapid cooling and avoid oxidation during cooling. The coatings were also wire-cut into 10 mm × 10 mm × 3 mm squares. For clarity, as-cast HEA, solution-treated HEA and FS HEA coatings were referred to as AC, ST and FSC, respectively. The samples for electrochemical testing were sealed with epoxy resin and ground from 240 grit to 800 grit to expose only one surface (10 mm × 10 mm). The samples for microstructure analysis were ground from 240 grit to 2000 grit gradually and mechanically polished to 0.5 μm with polishing compound. For EBSD detection, the samples were further polished with 50 nm silica polishing suspensions.

Table 1. The chemical composition of the as-cast CoCrFeMnNi HEA ingot (wt.%).

	Co	Cr	Fe	Mn	Ni	Rest
Nominal	21.02	18.55	19.91	19.59	20.93	0
XRF	20.20	18.75	20.80	19.08	21.02	0.15

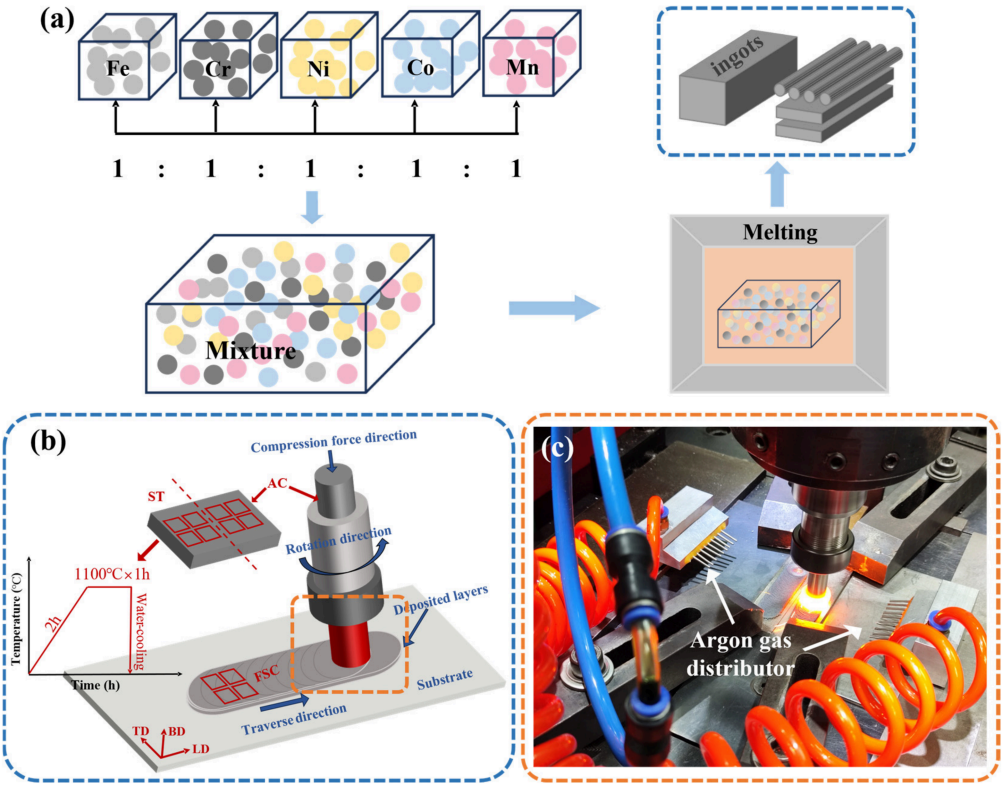


Figure 1. The schematic diagram of (**a**) HEA fabrication, (**b**) solution treatment and FS processing. (**c**) The setup of FS.

2.2. Surface Analysis

The microstructure and composition of various samples were obtained using the SEM (Gemini 500, Zeiss, Germany) coupled with an EDS detector (X-Man, Oxford, UK) and an EBSD detector (NordlysNano, Oxford, UK). The morphologies of three samples after immersion were also observed by SEM. The phase constituents were identified by XRD (D2, Bruker, Karlsruhe, Germany) with a scanning speed of 5°/min and a 2θ range of 10–90°. XPS (ESCALAB 250Xi, Thermo Fisher Scientific, Waltham, MA, USA) was conducted to analyze the composition of the passive film formed on different samples. All detected peaks were calibrated by the C 1s peak (284.8 eV). The spectra were analyzed using XPSpeak software (Version 4.1), and the fluctuation of peak position for the same substance was controlled within 0.1 eV to guarantee accurate quantitative analysis. The fitting FWHM was controlled within a reasonable range, not exceeding 2.5 eV.

2.3. Electrochemical Analysis

The electrochemical behavior was assessed using a conventional three-electrode system with an electrochemical workstation (Reference 600 Plus, Gamry, Warminster, PA, USA). A platinum foil (10 mm × 15 mm × 0.1 mm), a saturated calomel electrode (SCE) and a sealed sample (10 mm × 10 mm exposed area) served as the counter electrode, the reference electrode and the working electrode, respectively. All potentials were relative to SCE, and all tests were independently validated at least three times in this work. After immersion in 3.5 wt.% NaCl solution for 1 h, the open-circuit potential (OCP) was monitored for 1 h to ensure system stability. LPR was conducted from −10 mV to 10 mV vs. OCP at a scanning rate of 0.125 mV/s. EIS testing was then conducted with a 10 mV vs. OCP amplitude sinusoidal perturbation and a frequency range from 100 kHz to 10 mHz. The EIS spectra were fitted by ZSimpWin software (Version 3.50). PDP was conducted at a scanning rate of 1 mV/s from −0.3 V vs. OCP to anodic potential when the current density

reached 1 mA/cm^2. The corrosion current density (i_{corr}) was obtained by extrapolating the cathodic Tafel slope. According to the passive region determined from PDP curves, Mott-Schottky testing was conducted with a scanning range from −0.6 V to −0.1 V vs. SCE at a fixed frequency of 1000 Hz. The scanning voltage step was set at 50 mV, and the amplitude voltage was set at 5 mV.

3. Results and Discussion

3.1. Microstructures

Figure 2 depicts the SEM image and EDS results of the joint interface between the 304 stainless steel substrate and the CoCrFeMnNi HEA coating. SEM observation revealed no visible gaps at the joint interface, indicating a strong metallurgical bond between the coating and the substrate. In addition, upon observing the EDS mapping and line scanning results, the diffusion zone was evident at the joint interface. Across the diffusion zone from the 304 stainless steel substrate to the HEA coating, the Fe signal intensity gradually decreased, accompanied by a progressive increase in the Co, Ni and Mn signals. The Cr signal remained essentially unchanged, which was attributed to the similar Cr contents in both materials. No evident oxygen enrichment was observed at the interface. These observations indicated that, under the thermo-mechanical coupling imposed by FS, the HEA consumable rod underwent high-temperature plastic deformation and formed a distinct diffusion zone with the substrate, thereby promoting metallurgical bonding between the two.

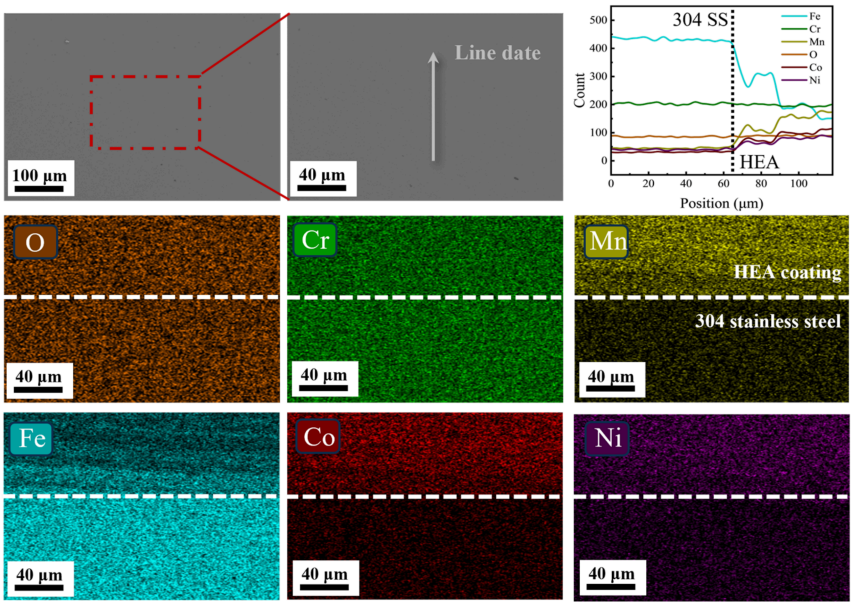


Figure 2. The SEM image of the joint interface between 304 stainless steel substrate and CoCrFeMnNi HEA coating, and the corresponding EDS mapping.

Figure 3 displays the inverse pole figures (IPF), grain boundary maps, kernel average misorientation (KAM) maps and corresponding detected EDS results. AC specimens exhibited a single-phase FCC structure with coarse grains, whose average equivalent circle diameter reached 230 μm (Figure 3(a1)). The grain boundaries were predominantly high-angle grain boundaries (HAGBs), accounting for over 98%. Dendritic segregation of Mn and Ni elements was observed. This was attributed to the lower binary enthalpy (ΔH_{mix}) of Mn and Ni, as shown in Table 2 [31,32]. A lower binary enthalpy indicates a stronger binding force between the two elements. After solution treatment, ST still remained a single FCC phase, and the grain size further coarsened to approximately 700 μm. The

dendritic structure in ST appeared more diffuse than that in AC, indicating that the solution treatment promoted the re-dissolution of Mn and Ni to a certain extent, but did not completely eliminate the segregation. The grain size of FSC was significantly refined to 6 μm, which was attributed to the SPD during FS (Figure 3(c1)). The fraction of low-angle grain boundaries (LAGBs) reached 24%. In addition, the fraction of Σ3 coincidence site lattice (CSL) boundaries, which are twin boundaries, reached 37% (Figure 3(c2)) [33]. These changes resulted from the dynamic recrystallization (DRX) upon cooling. KAM map shown in Figure 3(c3) revealed that high-density dislocations accumulate in the local fine-grained regions in FSC. Notably, the elemental distribution became homogeneous after FS and the dendritic segregation of Mn and Ni was eliminated.

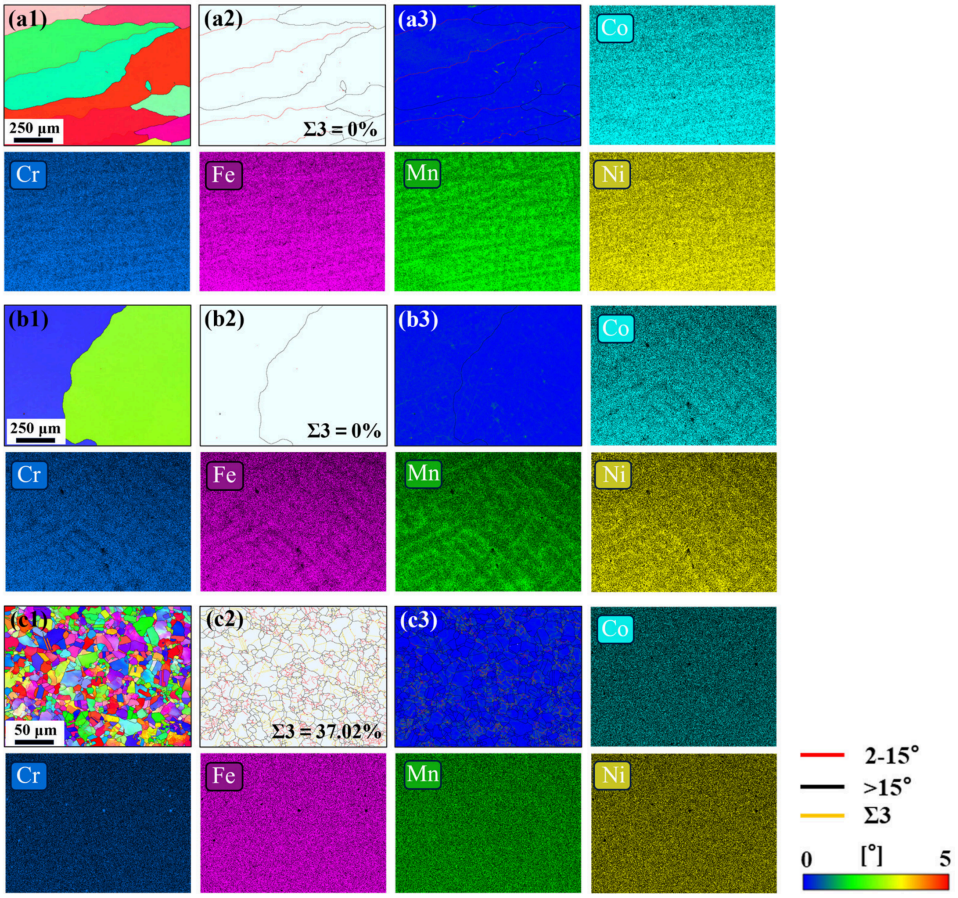


Figure 3. (**a1**,**b1**,**c1**) The IPF, (**a2**,**b2**,**c2**) grain boundary maps, (**a3**,**b3**,**c3**) KAM maps and corresponding EDS maps of (**a**) as-cast HEA (AC), (**b**) solution-treated HEA (ST) and (**c**) friction-surfaced HEA coating (FSC).

Table 2. Binary enthalpy (ΔH_{mix}) of different pairs of atoms in CoCrFeMnNi HEA (kJ/mol).

Element	Co	Cr	Fe	Mn	Ni
Co	-	−4	−1	−5	0
Cr		-	−1	2	−7
Fe			-	0	−2
Mn				-	−8
Ni					–

Figure 4 shows the XRD patterns of various specimens. The detected results showed that all specimens consisted of a single FCC solid solution structure. Compared with FSC, the characteristic peaks of the FCC structure in AC and ST exhibited noticeable asymmetry

and broadening. This was attributed to the severe dendritic segregation of Mn and Ni elements in AC and ST, which led to slight differences in lattice constant between the dendrite regions and interdendritic regions. These local variations in lattice parameter gave rise to microstrain increase and lattice distortion [34]. FS promoted the re-dissolution of Ni and Mn into the matrix, thereby eliminating local lattice differences.

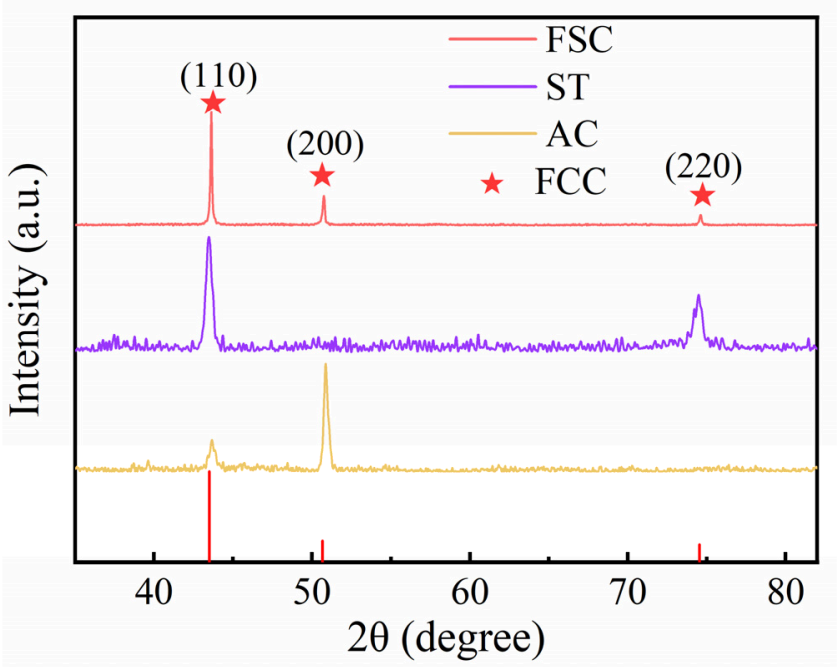


Figure 4. XRD patterns of AC, ST and FSC.

Figures 5 and 6 illustrate the morphology of inclusions in AC, ST and FSC. In AC (Figure 5) and ST (Figure 6a), the local aggregation of O and Cr elements could be observed. Line scanning results showed that the inclusion was mainly $(Cr, Mn)_xO_y$, and the inclusion size reached about 6.0 um and 5.5 um in AC and ST, respectively. According to previous studies, this inclusion was assumed to be $MnCr_2O_4$ with a spinel-type structure [35,36]. Pang et al. proposed that the Gibbs energies of formation (ΔG_f) of Mn_3O_4, $CoCr_2O_4$, $FeCr_2O_4$, $MnCr_2O_4$ and $NiCr_2O_4$ were −1042 kJ/mol, −1089 kJ/mol, −1121 kJ/mol, −1240 kJ/mol and −1042 kJ/mol at 1000 K, respectively [37]. Thus, compared with other oxides, $MnCr_2O_4$ shows the lowest ΔG_f, which means that it is thermodynamically more favorable to form preferentially and remain stable. Additionally, MnS precipitates were observed surrounding them, forming complex composite inclusions during cooling [38]. Following FS, S element segregation was virtually removed, and localized O element enrichment persisted. Line scanning results from Figure 6b revealed the absence of MnS accumulation around the $MnCr_2O_4$ inclusions, accompanied by a reduction in inclusion size to about 2.6 um. These findings demonstrated that FS not only promoted the chemical homogenization of the CoCrFeMnNi HEA, but also fragmented the inclusions through the induced SPD, leading to a reduction in point defects. It has been reported that $MnCr_2O_4$ and MnS inclusions markedly weaken the corrosion resistance due to the formation of local micro-galvanic coupling [39]. Accordingly, the influence of FS on the corrosion resistance of the CoCrFeMnNi HEA was further investigated.

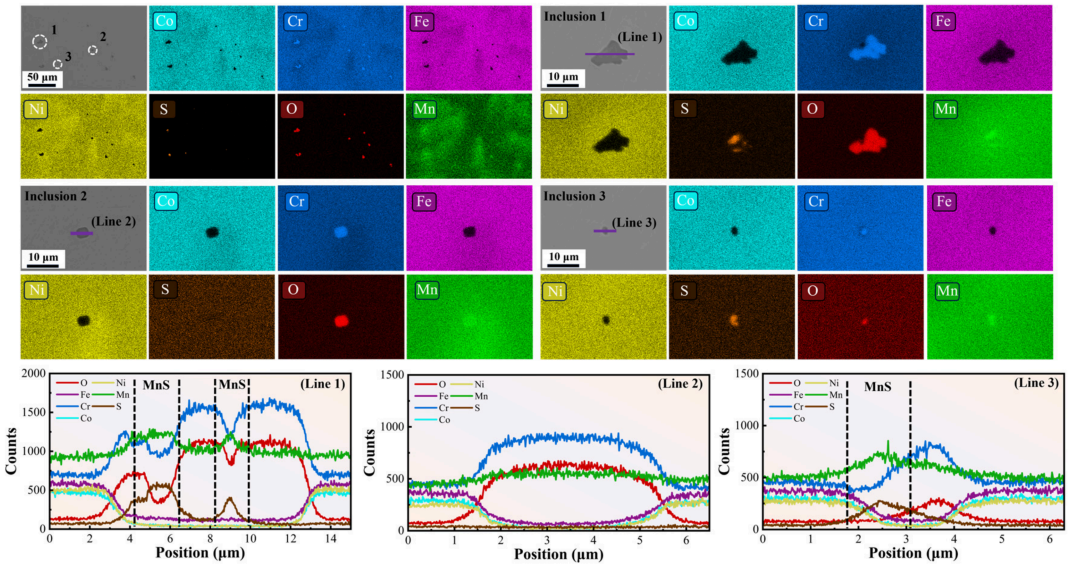


Figure 5. SEM images, corresponding EDS mappings and line scanning results of inclusions in AC.

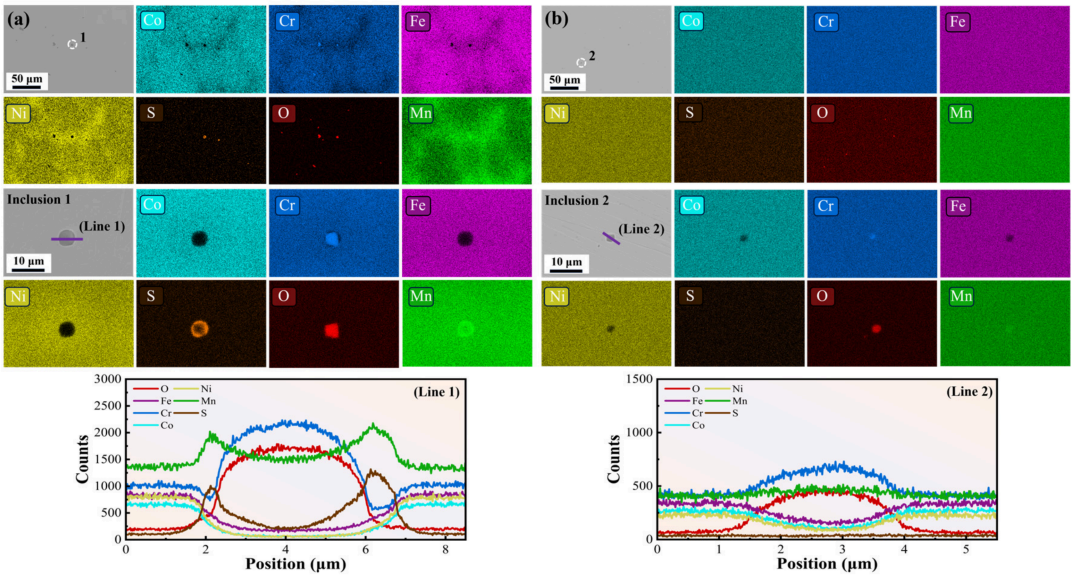


Figure 6. SEM images, corresponding EDS mappings and line scanning results of inclusions in (**a**) ST and (**b**) FSC.

3.2. Corrosion Behavior

Figure 7a displays the PDP curves of three specimens immersed in 3.5 wt.% NaCl solution for 2 h. The i_{corr} and E_{pit} determined from PDP curves are presented in Figure 7b. It can be seen from the curves that the anodic branches of AC and ST exhibited weak passivation behavior and lacked a well-defined passive current density. This was attributed to the severe dendritic segregation of Mn and Ni and the presence of inclusions, which compromised the integrity of the passive film. By contrast, ST showed a reduced i_{corr} of 0.23 μA/cm^2 and a positive shift in E_{corr}, indicating that the anodic reaction was predominantly suppressed. After FS, the HEA coating exhibited the lowest i_{corr} of 0.11 μA/cm^2 and the highest E_{pit} of 125.7 mV compared with AC and ST. Compared with ST, its anodic branch shifted more markedly toward lower current densities, indicating that the anodic reaction was further inhibited. It was worth noting that FSC exhibited an obvious passive region, suggesting the superior protective properties of the passive film. In addition, the 304 SS substrate showed i_{corr} of 0.13 μA/cm^2 and E_{pit} of 327.3 mV. The higher pitting potential of

304 SS compared with that of FSC was attributed to the lower density of point defects in its passive film, which made the film less susceptible to local breakdown and consequent failure. Polarization resistance (R_p) obtained from LPR testing is negatively correlated with the corrosion rate. Figure 7b shows the variation in R_p value for three samples. FSC achieved a significantly higher R_p value, meaning a lower corrosion rate in NaCl solution. The LPR results had a good correlation with the trend of i_{corr}.

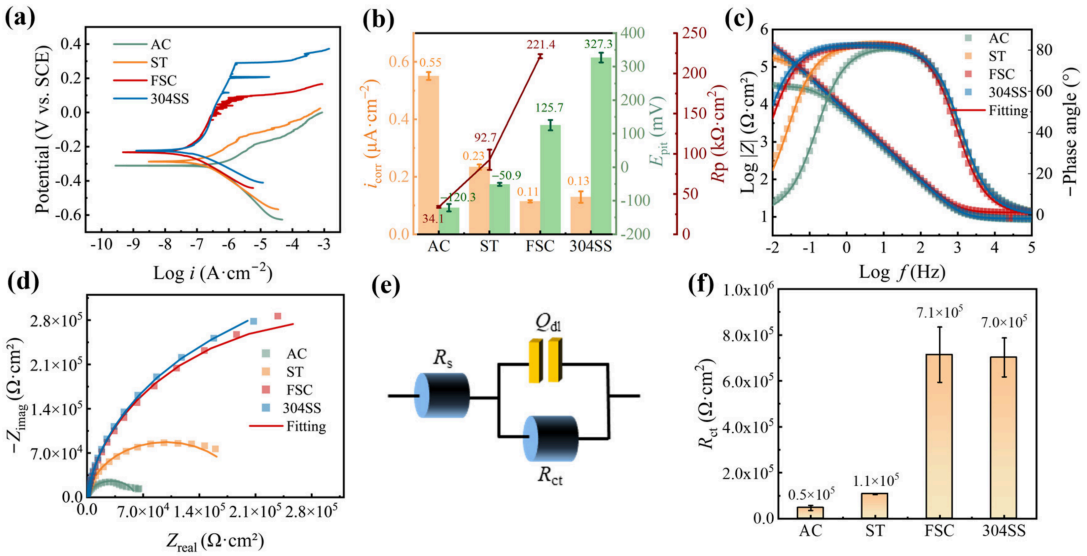


Figure 7. (**a**) PDP curves of various samples after 2 h of immersion in 3.5 wt.% NaCl solution. (**b**) LPR results and fitting i_{corr} and E_{pit} from PDP curves. (**c**) Bode and (**d**) Nyquist plots of three samples after 2 h of immersion in 3.5 wt.% NaCl solution. (**e**) The electrical equivalent circuit for the quantitative analysis and (**f**) the fitted R_{ct}.

Figure 7c,d exhibits the Bode plots and Nyquist plots of HEAs immersed in 3.5 wt.% NaCl solution for 2 h, respectively. The radius of the capacitive arc in the Nyquist plots for FSC was much larger than those of ST and AC, revealing enhanced corrosion resistance [40]. All curves of phase angle in Bode plots increased rapidly to about 80° and then decreased in the low-frequency region, showing only one time constant. Therefore, the electrical equivalent circuit shown in Figure 7e was employed to fit the EIS results. R_s represents the solution resistance, R_{ct} represents the charge transfer resistance, and Q_{dl} is the constant phase element (CPE) used to simulate the capacitance of the electrical double layer. Here, the CPE was utilized to fit non-ideal films instead of a pure capacitance. The impedance of the CPE is defined as follows [41]:

$$Z = \frac{1}{Q(jw)^n} \quad (1)$$

where Q is the magnitude of the CPE, j is the imaginary unit, w is the angular frequency, and n stands for the exponent constant of the CPE. The specific fitting parameters are listed in Table 3, and Figure 7f shows the R_{ct} value of each sample. The R_{ct} value of ST was more than two times that of AC, reaching 1.1×10^5 Ω·cm^2. It indicated that solution treatment slightly mitigated the dendritic segregation of Mn and Ni elements in the as-cast alloy, improving the electrochemical stability of the passive film. FSC exhibited an extremely high R_{ct} value of 7.1×10^5 Ω·cm^2. It confirmed that the SPD during FS eliminated the dendritic segregation and fragmented the coarse inclusions, thereby suppressing the initiation of localized corrosion due to micro-galvanic coupling. This resulted in a pronounced positive effect on the corrosion resistance enhancement. The fitted R_{ct} value for 304 SS was 7.0×10^5 Ω·cm^2, which was similar to that of FSC. It reflected that the passive films

spontaneously formed on the surfaces of both 304 SS and FSC in 3.5 wt.% NaCl solution possessed comparable resistance to chloride ion attack.

Table 3. Fitting parameters determined from the EIS results.

Sample	R_s ($\Omega \cdot cm^2$)	$Q_{dl} \times 10^{-5}$ ($\Omega^{-1} \cdot cm^{-2} \cdot s^n$)	n	$R_{ct} \times 10^5$ ($\Omega \cdot cm^2$)
AC	11.7 ± 1.4	3.4 ± 0.1	0.90 ± 0.01	0.5 ± 0.2
ST	8.7 ± 0.8	2.9 ± 0.1	0.91 ± 0.01	1.1 ± 0.1
FSC	12.0 ± 1.4	2.4 ± 0.1	0.93 ± 0.01	7.1 ± 1.2
304SS	8.9 ± 0.7	2.9 ± 0.1	0.92 ± 0.01	7.0 ± 0.9

3.3. Characterization of the Passive Film

The variation in semiconducting properties of the passive film formed on AC, ST and FSC was analyzed by Mott-Schottky testing, as shown in Figure 8. All cases in this work showed only one linear region with a negative slope, which reflected p-type semiconducting properties. The p-type semiconductors in the HEA passive film, with the main defect being cation vacancies, were related to Cr_2O_3, FeO, NiO, etc. The p–type semiconductor defect density (acceptor density) can be calculated as follows (per unit area of 1 cm^2) [42,43]:

$$\frac{1}{C^2} = -\frac{2}{\varepsilon \varepsilon_0 e N_A}\left(E - E_{FB} - \frac{kT}{e}\right) \quad (2)$$

where ε stands for the relative dielectric constant of the passive film (generally 15.6) [5]; ε_0 is the vacuum permittivity (8.854 × 10^{-14} F·cm^{-1}); e represents the electron charge (1.602 × 10^{-19} C); N_A is the acceptor density. According to the slope from C^{-2}-E curves, N_A values of various specimens were determined. The N_A value of AC was 4.2 × 10^{20} cm^{-3} and decreased to 2.1 × 10^{20} cm^{-3} after solution treatment, suggesting a lower defect density in the passive film of ST. FSC showed the lowest N_A value of 1.0 × 10^{20} cm^{-3}, implying that the passive film formed on the FSC surface was more compact, less defective, and therefore possessed superior protective properties. These results were consistent with the electrochemical analysis. It further suggested that FS processing reduced the defect density of the passive film by promoting chemical homogenization and fragmenting inclusions, resulting in a marked improvement in corrosion resistance.

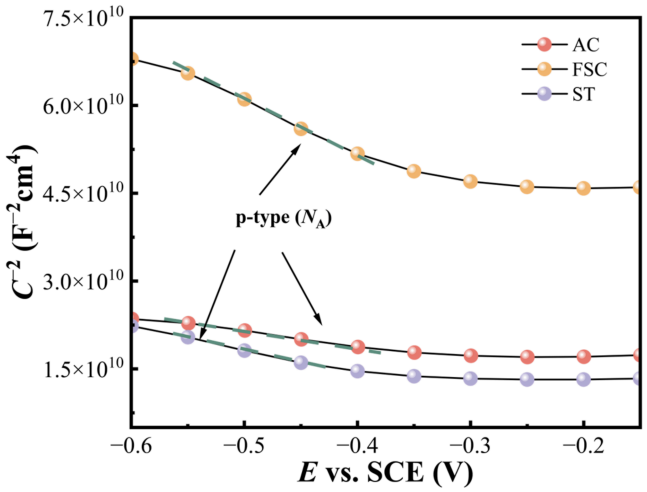


Figure 8. Mott-Schottky diagram of AC, ST and FSC after 2 h of immersion in 3.5 wt.% NaCl solution.

To further reveal the composition variation in the passive film formed on different samples, high-resolution XPS spectra of Co $2p_{3/2}$, Cr $2p_{3/2}$, Fe $2p_{3/2}$, Mn $2p_{3/2}$ and Ni

$2p_{3/2}$ peaks were analyzed, as shown in Figure 9. The corresponding binding energy of each element is listed in Table 4 [21,44,45]. The proportions of metallic elements of Co^0, Cr^0, Fe^0, Mn^0 and Ni^0 in FSC were lower than those in AC and ST. This was attributed to the thicker passive film formed on the surface of FSC. The detection depth of XPS is about 1~6 nm [44]. Compared to Co^0, Mn^0 and Ni^0, the fractions of Cr^0 and Fe^0 in all three HEAs were much lower, demonstrating that the oxides and hydroxides of Cr and Fe are the predominant constituents of the passive film. The values of Fe_{hy}/Fe_{ox} and Cr_{hy}/Cr_{ox} are generally negatively correlated with the stability of the passive film, due to the weaker stability of Fe hydroxides and Cr hydroxides. The Fe_{hy}/Fe_{ox} ratios of AC, ST and FSC were 1.00, 0.89 and 0.79, respectively. The Cr_{hy}/Cr_{ox} ratios of AC, ST and FSC were 1.39, 0.58 and 0.58, respectively. The variation in Fe_{hy}/Fe_{ox} ratio and Cr_{hy}/Cr_{ox} ratio between ST and FSC was limited, and the highest Fe_{hy}/Fe_{ox} and Cr_{hy}/Cr_{ox} ratios of AC revealed poor corrosion resistance of the passive film. These findings followed that solution-treatment and FS processing could promote thickening of the passive film on the CoCrFeMnNi HEA. In addition, the formation of stable components of Cr oxides and Fe oxides was also facilitated, resulting in a decrease in the defects in the passive film (Figure 8) and the enhanced corrosion resistance (Figure 7).

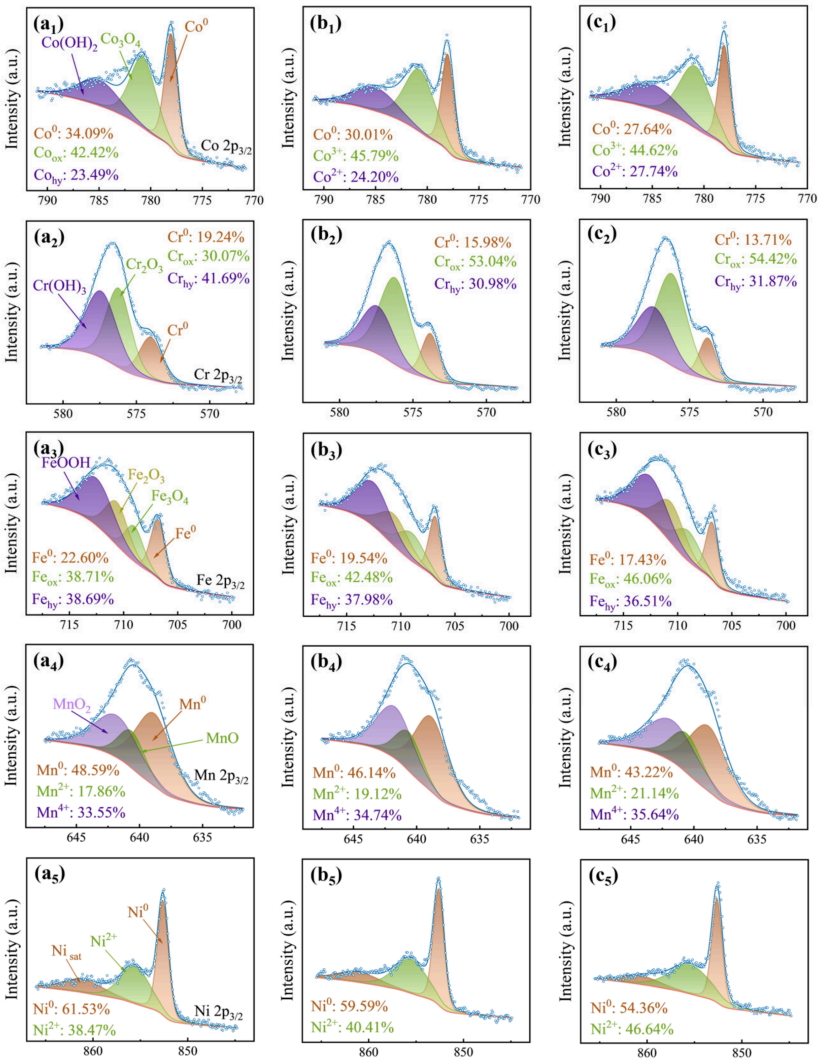


Figure 9. High-resolution XPS spectra of Co $2p_{3/2}$, Cr $2p_{3/2}$, Fe $2p_{3/2}$, Mn $2p_{3/2}$ and Ni $2p_{3/2}$ for (**a**) AC, (**b**) ST and (**c**) FSC.

Table 4. The binding energies of the main components of the passive film from XPS.

Element	Peak	Binding Energy (eV)	Element	Peak	Binding Energy (eV)
Co $2p_{3/2}$	Co^0	778.0 ± 0.1	**Cr $2p_{3/2}$**	Cr^0	573.7 ± 0.1
	Co_3O_4	780.7 ± 0.1		Cr_2O_3	576.2 ± 0.1
	$Co(OH)_2$	785.0 ± 0.1		$Cr(OH)_3$	577.4 ± 0.1
Fe $2p_{3/2}$	Fe^0	706.8 ± 0.1	**Mn $2p_{3/2}$**	Mn^0	638.8 ± 0.1
	Fe_3O_4	709.0 ± 0.1		MnO	640.5 ± 0.1
	Fe_2O_3	710.6 ± 0.1		MnO_2	641.7 ± 0.1
	FeOOH	712.5 ± 0.1	**Ni $2p_{3/2}$**	Ni^0	852.6 ± 0.1
				Ni^{2+}	855.4 ± 0.1
				Ni sat	861.0 ± 0.1

3.4. Corrosion Morphology

Figure 10 shows the corrosion morphology of three samples and EDS mappings. MnS inclusions usually behave as an anodic phase in passive alloys, leading to their preferential dissolution [46]. $MnCr_2O_4$ acts as a cathodic phase due to its high stability. Therefore, the signal of $MnCr_2O_4$ could be observed around the corrosion pits, whereas no accumulation of S signal was detected. Moreover, the presence of inclusion signals around the pits in all three specimens suggested that pitting preferentially nucleated at inclusion sites. In FSC (Figure 10c), the surface morphology remained relatively intact, with small-sized corrosion pits compared to AC and ST, demonstrating higher corrosion resistance to Cl^-. These results highlighted the importance of FS-induced inclusion fragmentation in the improved corrosion performance.

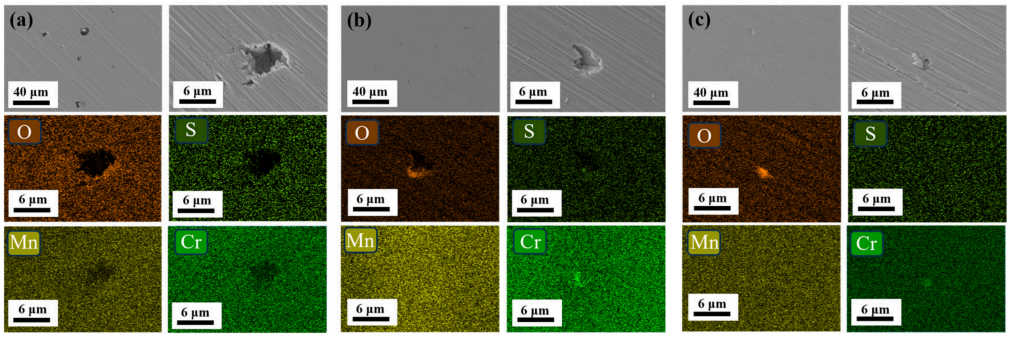


Figure 10. Corrosion morphology of (**a**) AC, (**b**) ST and (**c**) FSC after immersion and corresponding EDS mappings.

4. Conclusions

In summary, this work successfully fabricated the CoCrFeMnNi high-entropy alloy (HEA) coating via friction surfacing (FS). The effect of FS and solution treatment on the microstructural evolution and corrosion behavior of as-cast CoCrFeMnNi HEA was systematically investigated. Several key conclusions were drawn as follows:

(1) Compared with solution treatment, FS eliminated the dendritic segregation of Mn and Ni elements in the CoCrFeMnNi HEA and simultaneously fragmented the $MnCr_2O_4$ as well as MnS inclusions. Furthermore, through severe plastic deformation and dynamic recrystallization, the grain size was refined from ~230 μm in the as-cast state to ~6 μm.

(2) Electrochemical testing results demonstrated that the FSed-coating exhibited the lowest i_{corr} of 0.11 μA/cm^2, the highest E_{pit} of 125.7 mV and the largest R_{ct} of 7.1×10^5 Ω·cm^2 in 3.5 wt.% NaCl solution, indicating that FS significantly enhanced the corrosion resistance of the CoCrFeMnNi HEA.

(3) Mott-Schottky and XPS analyses revealed that FS fragmented the inclusions and promoted the chemical homogeneity of the passive film, thereby reducing point defects in the passive film and consequently enhancing its compactness and protective capability.

This research is the first systematic study to reveal the effect of FS on microstructural evolution and corrosion behavior of CoCrFeMnNi HEA coating, which fills the gap regarding how FS-induced grain refinement, inclusion fragmentation and chemical homogenization affect the corrosion resistance of HEA. However, this study also presents limitations. Due to the poor thermal conductivity of CoCrFeMnNi HEA, continuous coating formation relying on friction-generated heat is difficult, resulting in a narrow processing window. Future work should therefore focus on tailoring HEA compositions to improve thermal conductivity and systematically exploring the influence of FS processing parameters on FSed HEA coating performance.

Author Contributions: Conceptualization, W.C., H.Q., C.T.K. and L.M.T.; Methodology, W.C., F.Y., M.Z., D.G., T.S. and D.Z.; Validation, D.G.; Investigation, W.C., F.Y., J.R., Z.W., M.Z. and H.Z.; Data curation, W.C., F.Y., J.R., Z.W. and H.Z.; Writing—original draft, W.C.; Writing—review and editing, H.Q., D.G., T.S., C.T.K. and L.M.T.; Supervision, H.Q., T.S., C.T.K., L.M.T. and D.Z. All authors have read and agreed to the published version of the manuscript.

Funding: This research was funded by the Advanced Materials-National Science and Technology Major Project (No. 2024ZD0607500), the National Key R&D Program of China (2023YFE0205300), the Interdisciplinary Research Project for Young Teachers of USTB (Fundamental Research Funds for the Central Universities, FRF-IDRY-25-027) and the Guangdong Basic and Applied Basic Research Foundation (2021B1515130009).

Institutional Review Board Statement: Not applicable.

Informed Consent Statement: Not applicable.

Data Availability Statement: The original contributions presented in this study are included in the article material. Further inquiries can be directed to the corresponding authors.

Conflicts of Interest: Authors Min Zhou, Dawei Guo and Lap Mou Tam were employed by the company IDQ Science and Technology Development (Hengqin, Guangdong) Co. Ltd. The remaining authors declare that the research was conducted in the absence of any commercial or financial relationships that could be construed as a potential conflict of interest.

References

1. Refait, P.; Paul, S. New frontiers in marine corrosion research. *npj Mater. Degrad.* **2025**, *9*, 11. [CrossRef]
2. Lawal, S.L.; Afolalu, S.A.; Jen, T.C.; Akinlabi, E.T. Corrosion control and its application in marine environment—A review. *Solid State Phenom.* **2024**, *355*, 61–73. [CrossRef]
3. Dalmora, G.P.V.; Filho, E.P.B.; Conterato, A.A.M.; Roso, W.S.; Pereira, C.E.; Dettmer, A. Methods of corrosion prevention for steel in marine environments: A review. *Results Surf. Interfaces* **2025**, *18*, 100430. [CrossRef]
4. Li, H.; Meng, X.Z.; Yan, H.J.; Zheng, R.C.; Hu, H.S.; Lei, B.; Zhang, Q.H.; Wu, L.K. Intelligent marine waterborne epoxy coating based on functionalized multiscale nanocomposite: Mechanical enhancement, self-reporting, and active/passive anti-corrosion. *J. Mater. Sci. Technol.* **2024**, *221*, 68–83. [CrossRef]
5. Ye, Y.; Wang, Q.; Lu, J.; Liu, C.; Yang, Y. High-entropy alloy: Challenges and prospects. *Mater. Today* **2016**, *19*, 349–362. [CrossRef]
6. Gan, S.; Xu, Q.; Zhang, Y.; Singh, B.S.B. Effect of $AlCoCrFeNi_{2.1}$ high-entropy alloy reinforcement on the densification, microstructure, and hot-cracking behavior of LPBF-processed AA7075. *Metals* **2025**, *15*, 1193. [CrossRef]
7. Zhou, Y.; Zhao, R.; Ren, B.; Jiang, A.; Liu, Z.; Liu, J. Influence of Si content on microstructure and mechanical properties of CoCrFeNi high-entropy alloys. *Metals* **2025**, *15*, 538. [CrossRef]
8. Yeh, J.W.; Yeh, A.C.; Hsu, W.L. High-Entropy Alloys. In *Physical Metallurgy*; Elsevier: Amsterdam, The Netherlands, 2026; pp. 2205–2250. [CrossRef]
9. Balaji, V.; Anthony, X.M. Development of high entropy alloys (HEAs): Current trends. *Heliyon* **2024**, *10*, e26464. [CrossRef]

10. Liang, J.; Zhu, G.; Sun, J.; Qu, S.; Jiang, J.; Cao, G.; Wang, H.; Shen, J.; Feng, A.; Chen, D. Influence of heat treatment on the microstructure and mechanical properties of FeCoNiCrMn high-entropy alloy manufactured via laser powder bed fusion. *Metals* **2025**, *15*, 260. [CrossRef]
11. Atabay, S.E.; Sarafan, S.; Islam, A.; Bernier, F.; Gholipour, J.; Amos, R.; Patnaik, P.; Wanjara, P.; Brochu, M. Laser powder bed fusion printing of CoCrFeMnNi high entropy alloy: Processing, microstructure, and mechanical properties. *High Entropy Alloys Mater.* **2024**, *2*, 129–173. [CrossRef]
12. Konovalov, S.; Gudala, S.; Panchenko, I.; Osintsev, K.; Chen, X. Evolution of microstructure, mechanical properties and phase stability of CoCrFeMnNi high entropy alloys. *Vacuum* **2024**, *227*, 113405. [CrossRef]
13. Laplanche, G.; Berglund, S.; Reinhart, C.; Kostka, A.; Fox, F.; George, E.P. Phase stability and kinetics of σ-phase precipitation in CrMnFeCoNi high-entropy alloys. *Acta Mater.* **2018**, *161*, 338–351. [CrossRef]
14. Zhang, X.; Jiang, Z.; Chen, H.; Niu, M.; Cheng, J. Mechanical properties of CoCrFeNi-X (X = Ti, Sn) high entropy alloy and tribological properties in simulated seawater environment. *Tribol. Int.* **2025**, *202*, 110306. [CrossRef]
15. Lee, J.; Park, C.; Park, H.; Kang, N. Effective hydrogen diffusion coefficient for CoCrFeMnNi high-entropy alloy and microstructural behaviors after hydrogen permeation. *Int. J. Hydrogen Energy* **2020**, *45*, 10227–10232. [CrossRef]
16. Kwak, J.; Son, S.; Jung, S.M.; Lee, J.; Kim, K.S.; Lee, B.J.; Kim, H.S.; Kim, Y.T. Enhanced Corrosion Resistance of Equiatomic CoCrFeMnNi High-Entropy Alloy via Chromium Enrichment in the Oxide Layer Induced by Cathodic Modification. *J. Mater. Res. Technol.* **2026**, *41*, 1580–1590. [CrossRef]
17. Lee, D.W.; Lee, J.A.; Park, H.; Kim, R.E.; Choe, J.; Hong, S.I.; Kim, H.S. Leveraging microstructural design to enhance strain hardening in porous CoCrFeMnNi high-entropy alloy fabricated by material extrusion additive manufacturing. *Mater. Sci. Eng. A* **2025**, *940*, 148579. [CrossRef]
18. Zhang, H.; Ma, H.; Li, C.; Cao, S.; Liu, C.; Huang, P.; Fan, Z.; Li, J. Revealing defect-structure-performance relationship of CoCrFeMnNi high-entropy alloy manufactured by laser-based powder bed fusion. *Mater. Sci. Eng. A* **2025**, *948*, 149333. [CrossRef]
19. Liu, S.; Hu, M.; Meng, Y.; Xiao, L.; Song, W. Strain-rate-driven shear mechanisms in additively manufactured CoCrFeMnNi chemically complex alloys. *J. Mater. Res. Technol.* **2025**, *138*, 1145–1153. [CrossRef]
20. Ye, Q.; Feng, K.; Li, Z.; Lu, F.; Li, R.; Huang, J.; Wu, Y. Microstructure and corrosion properties of CrMnFeCoNi high entropy alloy coating. *Appl. Surf. Sci.* **2017**, *396*, 1420–1426. [CrossRef]
21. Xu, Z.; Zhang, H.; Du, X.; He, Y.; Luo, H.; Song, G.; Mao, L.; Zhou, T.; Wang, L. Corrosion resistance enhancement of CoCrFeMnNi high-entropy alloy fabricated by additive manufacturing. *Corros. Sci.* **2020**, *177*, 108954. [CrossRef]
22. Chang, W.; Tian, Z.; Jiang, F.; Zhou, M.; Guo, D.; Gao, J.; He, S.; Kwok, C.T.; Tam, L.M.; Qian, H.; et al. Microbial corrosion of CoCrMnNi high entropy alloy by Pseudomonas aeruginosa through electron transfer between Mn and microbe. *J. Mater. Res. Technol.* **2024**, *29*, 386–399. [CrossRef]
23. Nakama, D.; Katoh, K.; Tokisue, H. Some characteristics of AZ31/AZ91 dissimilar magnesium alloy deposit by friction surfacing. *Mater. Trans.* **2008**, *49*, 1137–1141. [CrossRef]
24. Bararpour, S.M.; Aval, H.J.; Jamaati, R.; Fathy, A. Enhanced microstructure and Tribological performance of friction-surfaced A390 aluminum coatings via underwater burnishing. *Surf. Coat. Technol.* **2026**, *531*, 133370. [CrossRef]
25. Guo, D.; Kwok, C.T.; Chan, S.L.I.; Tan, L.M. Friction surfacing of AISI 904L super austenitic stainless steel coatings: Microstructure and properties. *Surf. Coat. Technol.* **2021**, *408*, 126811. [CrossRef]
26. Chang, W.; Gao, J.; Qian, H.; Guo, D.; Zhou, M.; Lou, Y.; Lam, W.I.; Kwok, C.T.; Tam, L.M.; Zhang, D. Microbiologically influenced corrosion of friction-surfaced 630 stainless steel coating in the presence of *Pseudomonas aeruginosa*. *Corros. Sci.* **2025**, *245*, 112708. [CrossRef]
27. Wu, D.; Li, J.; Wang, X.; Tang, W.; Liu, S.; Hou, J. Microstructure evolution and excellent strength and ductility properties of Mg–Gd–Y–Zr alloys prepared by additive friction stir deposition. *Prog. Addit. Manuf.* **2026**. [CrossRef]
28. Nahr, M.A.; Mirsalehi, S.E.; Papi, A. Additive manufacturing of AA2024/Al_2O_3 nanocomposites via friction surfacing: Investigating metallurgical, mechanical, and tribological properties. *J. Mater. Res. Technol.* **2025**, *36*, 8609–8631. [CrossRef]
29. Guo, D.; Chen, J.; Chen, X.; Shi, Q.; Cristino, V.A.M.; Kwok, C.T.; Tam, L.M.; Qian, H.; Zhang, D.; Li, X. Pitting corrosion behavior of friction-surfaced 17-4PH stainless steel coatings with and without subsequent heat treatment. *Corros. Sci.* **2021**, *193*, 109887. [CrossRef]
30. Nartu, M.S.K.K.Y.; Garcia, D.; Meher, S.; Wang, T.; Santos, J.F.D.; Rooyen, I.V. Friction surface layer deposition of triple-phase Al10Cr12Fe35Mn23Ni20 high entropy alloy: Process optimization and microstructural evolution. *Mater. Sci. Eng. A* **2025**, *927*, 148019. [CrossRef]
31. Takeuchi, A.; Inoue, A. Classification of bulk metallic glasses by atomic size difference, heat of mixing and period of constituent elements and its application to characterization of the main alloying element. *Mater. Trans.* **2025**, *46*, 2817–2829. [CrossRef]
32. Su, R.; Mi, M.; Shen, Z.; Qin, X.; Jia, Y.; Mu, Y.; Jiang, Z. Elemental Segregation Behavior and Cryogenic Strength-Ductility Synergy in Additively Manufactured FeCrNiMn Multi-Principal Element Alloy. *J. Mater. Res. Technol.* **2026**, *44*, 6074–6086. [CrossRef]

33. Zhou, M.; Shi, Q.; Chang, W.; Qian, H.; Guo, D.; Zhang, D.; Kwok, C.T.; Li, X.; Tam, L.M. Improvement of cavitation erosion resistance of lean grade austenitic stainless steels by friction surfacing. *Mater. Chem. Phys.* **2025**, *344*, 131144. [CrossRef]
34. Andrade, A.B.; Ferreira, N.S.; Valerio, M.E.G. Particle size effects on structural and optical properties of BaF_2 nanoparticles. *RSC Adv.* **2017**, *7*, 26839–26848. [CrossRef]
35. Andrews, N.A.; Barton, M.A.; Yang, S.M.; Park, T.; Noh, S.; Chang, H.J.; Kim, J.H. Effect of radio-frequency plasma spheroidization on the microstructure and mechanical properties of 10Cr ferritic oxide dispersion-strengthened steel. *Mater. Sci. Eng. A* **2023**, *863*, 144528. [CrossRef]
36. Zhang, X.; Zhao, Q.; Liu, C.; Peng, Y.; Huang, Y.; Kong, J.; Wang, K. On the formation of oxide inclusions in the high nitrogen chromium-manganese steel produced by the Wire and Arc Additive Manufacturing. *J. Mater. Res. Technol.* **2024**, *33*, 3852–3863. [CrossRef]
37. Pang, J.; Xiong, T.; Wei, X.; Zhu, Z.; Zhang, B.; Zhou, Y.; Shao, X.; Jin, Q.; Zheng, S.; Ma, X. Oxide $MnCr_2O_4$ induced pitting corrosion in high entropy alloy CrMnFeCoNi. *Materialia* **2019**, *6*, 100275. [CrossRef]
38. Zhang, X.; Peng, X.; Huang, Y.; Wang, K.; Kong, J.; Du, Z.; Wu, T. Precipitation characteristics and tensile properties of high-nitrogen chromium-manganese steel fabricated by wire and arc additive manufacturing with isothermal post-heat treatment. *Mater. Des.* **2023**, *225*, 111536. [CrossRef]
39. Zheng, S.; Wang, Y.; Zhang, B.; Zhu, Y.; Liu, C.; Hu, P.; Ma, X. Identification of $MnCr_2O_4$ nano-octahedron in catalysing pitting corrosion of austenitic stainless steels. *Acta Mater.* **2010**, *58*, 5070–5085. [CrossRef]
40. Lv, J.; Guo, Y.; Cao, Y.; Zhou, Z. Mechanical properties and corrosion resistance of wrought and laser powder-bed fusion CoCrNi medium entropy alloys. *J. Alloys Compd.* **2025**, *1035*, 181499. [CrossRef]
41. Luo, X.; Zhang, J.; Chou, T.; Gan, J.; Ju, J.; Zhou, Y.; Yang, T. Simultaneous improvement of mechanical properties and corrosion resistance of D019-strengthened high-entropy alloys via tailored microstructures. *Corros. Sci.* **2025**, *256*, 113193. [CrossRef]
42. Pu, Y.; Dou, W.; Cheng, Y.; Chen, S.; Xu, Z.; Chen, Z. Biogenic H_2S and extracellular electron transfer resulted in two-coexisting mechanisms in 90/10 Cu-Ni alloy corrosion by a sulfate-reducing bacteria. *Corros. Sci.* **2023**, *211*, 110911. [CrossRef]
43. Lian, C.; Xie, W.; Fang, H.; Wang, W.; Yu, J.; Li, J.; He, X. Effect of Cr: Al ratio on corrosion mechanism of Ni-Cr-Mo-Al alloys in 3.5 wt.% NaCl solution: Microstructure and electrochemical and passive characteristics. *Materials* **2025**, *18*, 2177. [CrossRef]
44. Lou, Y.; Dai, C.; Chang, W.; Qian, H.; Huang, L.; Du, C.; Zhang, D. Microbiologically influenced corrosion of $FeCoCrNiMo_{0.1}$ high-entropy alloys by marine *Pseudomonas aeruginosa*. *Corros. Sci.* **2019**, *165*, 108390. [CrossRef]
45. Li, Z.; Lei, H.; Dong, H.; Chiang, F.K.; Wang, X.; Zhang, G.; Wang, H.; Wu, Y.; Jiang, S.; Zhang, X.; et al. Positive-enthalpy-driven phase-selective dealloying for nanoporous high-entropy amorphous phosphide electrocatalysts toward efficient bifunctional water splitting. *Mater. Today Energy* **2026**, *58*, 102267. [CrossRef]
46. Liu, C.; Li, X.; Revilla, R.I.; Sun, T.; Zhao, J.; Zhang, D.; Yang, S.; Liu, Z.; Cheng, X.; Terryn, H.; et al. Towards a better understanding of localised corrosion induced by typical non-metallic inclusions in low-alloy steels. *Corros. Sci.* **2021**, *179*, 109150. [CrossRef]

Disclaimer/Publisher's Note: The statements, opinions and data contained in all publications are solely those of the individual author(s) and contributor(s) and not of MDPI and/or the editor(s). MDPI and/or the editor(s) disclaim responsibility for any injury to people or property resulting from any ideas, methods, instructions or products referred to in the content.